AGU PUBLICATIONS

JGR

Journal of Geophysical Research: Oceans

RESEARCH ARTICLE

10.1002/2014JC010393

**Key Points:**
- Documents the highly variable morphologies and properties of the NLIWs
- NLIWs are possibly generated by shoaling of a remotely incident internal tide
- NLIWs suggest an important contributor to local cross-shore transport

**Correspondence to:**
S. Zhang,
shzhang@apl.washington.edu

**Citation:**
Zhang, S., M. H. Alford, and J. B. Mickett (2015), Characteristics, generation and mass transport of nonlinear internal waves on the Washington continental shelf, *J. Geophys. Res. Oceans*, *120*, 741–758, doi:10.1002/2014JC010393.

Received 29 AUG 2014
Accepted 24 DEC 2014
Accepted article online 7 JAN 2015
Published online 12 FEB 2015

# Characteristics, generation and mass transport of nonlinear internal waves on the Washington continental shelf

**Shuang Zhang[1,2], Matthew H. Alford[2,3], and John B. Mickett[1]**

[1]Applied Physics Laboratory, University of Washington, Seattle, Washington, USA, [2]School of Oceanography, University of Washington, Seattle, Washington, USA, [3]Scripps Institution of Oceanography, La Jolla, California, USA

**Abstract** As a step toward better understanding the generation of nonlinear internal waves (NLIWs) on continental shelves and the factors determining their morphology, amplitude and propagation, we analyze more than 1500 NLIWs detected on the Washington (WA) continental shelf using four summer/fall time series of temperature and velocity measurements from a surface mooring deployed in 100 m of water. Propagating onshore toward the northeast, these NLIWs take a variety of forms, including internal solitary waves, solitary wave trains and bores. Nearly all are mode-1 depression waves that arrive semidiurnally along with the internal tide. The NLIW energy flux is correlated with the internal tide energy flux but not the local barotropic forcing, implying that the observed NLIWs arise primarily from shoaling remotely generated internal tides rather than local generation. Estimated onshore transport by the waves can equal or exceed offshore Ekman transport, suggesting the waves may play an important role in the mass balance on the continental shelf.

## 1. Introduction

Nonlinear internal waves (NLIWs) have been detected around the globe with a wide variety of in situ and remote techniques as reviewed by *Ostrovsky and Stepanyants* [1989] and *Apel et al.* [2006]. Recent observational studies of NLIWs on continental shelf regions such as the Oregon coast [*Stanton and Ostrovsky*, 1998; *Klymak and Moum*, 2003; *Moum et al.*, 2007a, 2007b; *D'Asaro et al.*, 2007], the New Jersey coast [*Shroyer et al.*, 2010a, 2011], Massachusetts Bay [*Scotti et al.*, 2006, 2008], and the South China Sea [*Duda et al.*, 2004; *Klymak et al.*, 2006; *Alford et al.*, 2010; *Lien et al.*, 2012] show that NLIWs in coastal oceans are frequent and energetic. They have been observed to transport energy [e.g., *Moum et al.*, 2007b; *D'Asaro et al.*, 2007] and mass [e.g., *Inall et al.*, 2001; *Shroyer et al.*, 2010b], and to serve as an effective mechanism for mixing [e.g., *MacKinnon and Gregg*, 2003; *Moum et al.*, 2007a], making them a potential contributor to vertical nutrient and heat flux over the shelf [e.g., *Shroyer et al.*, 2010b]. For these reasons, NLIWs can also affect biological distributions [e.g., *Pineda*, 1991; *Scotti and Pineda*, 2007], sediment resuspension [e.g., *Bogucki et al.*, 1997; *Klymak and Moum*, 2003] and underwater acoustics [*Apel et al.*, 2006].

In coastal oceans, NLIWs are usually believed to be generated either by (i) the release of internal lee waves or hydraulic jumps generated by barotropic tidal flow over topographic features [e.g., *Lee and Beardsley*, 1974; *Farmer and Smith*, 1980; *Maxworthy*, 1980; *Farmer and Armi*, 1999]; or (ii) nonlinear transformation of the baroclinic (internal) tide as it propagates over slope-shelf topography [e.g., *Gerkema*, 1995; *Colosi et al.*, 2001; *Lien et al.*, 2005; *Helfrich and Grimshaw*, 2008; *Alford et al.*, 2010; *Nash et al.*, 2012]. In mechanism (ii), internal tides in coastal regions usually come from multiple locations [e.g., *Nash et al.*, 2012; *Alford et al.*, 2012], possibly including remote and local sources. A superposition of multiple internal tides may produce NLIWs with mixed properties and result in no particular phase relationship with the barotropic tide [*Inall et al.*, 2000; *Nash et al.*, 2012]. Additionally, variations in phasing between internal/barotropic tides and their oblique angle of incidence on the irregularly shaped continental shelf would be expected to modulate the formation, shape and propagation of the waves.

NLIWs can take a large variety of shapes and properties, including bores, undular bores, solitary waves, and wave trains [e.g., *Ostrovsky*, 1978; *Gerkema*, 1995; *Henyey*, 1999; *Stepanyants*, 2006]. The morphology and evolution of NLIWs have been analyzed in previous numerical and laboratory studies [e.g., *Maxworthy*, 1980; *Helfrich and Melville*, 1986], but the factors determining the shape and size of NLIWs are poorly understood.

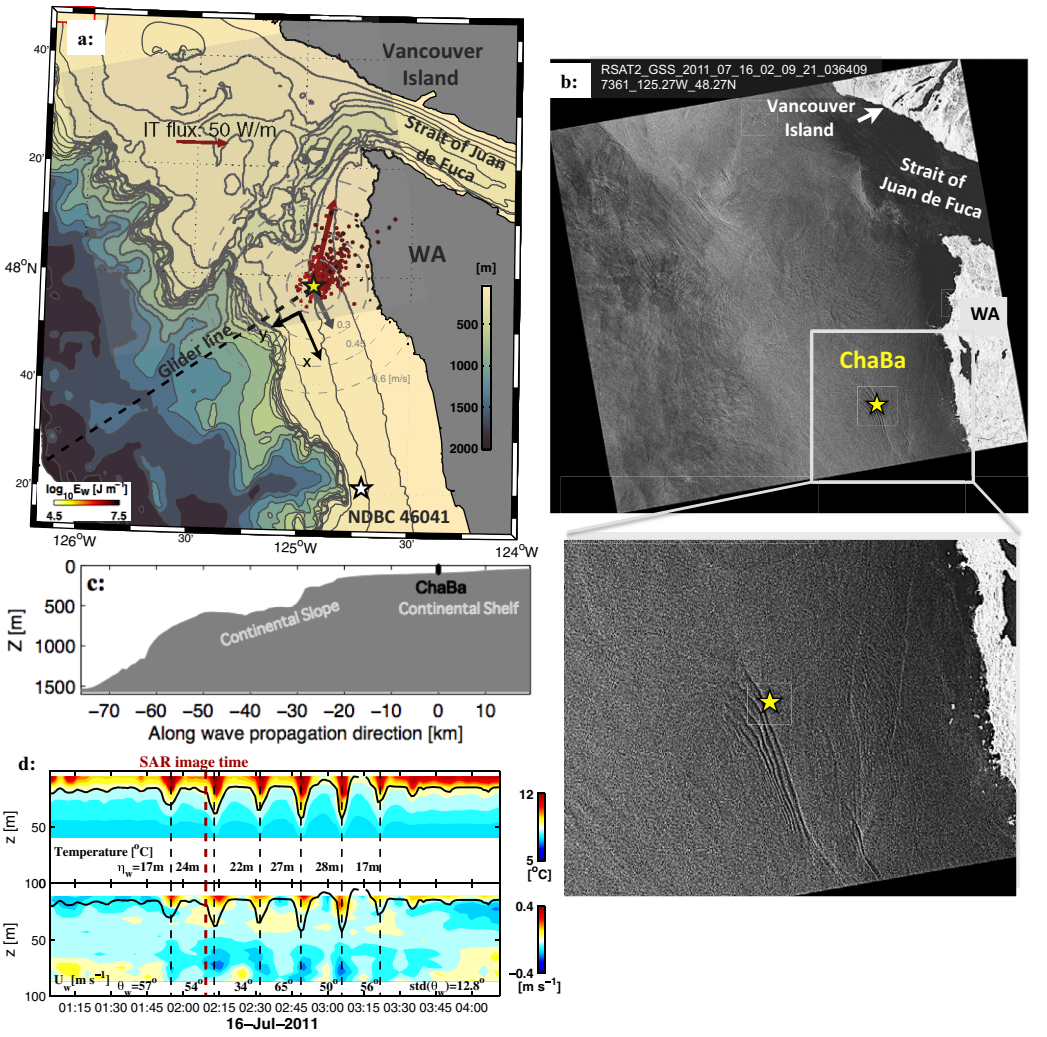


**Figure 1.** (a) Site map showing bathymetric features, along with *ChaBa* mooring (yellow star), NDBC buoy (white star), time-mean semi-diurnal mode-1 internal tide energy flux $F_{IT}$ (red arrow) and the Seaglider SG187 line (black dashed line) across the continental slope/shelf. Along-shore flow (gray arrow, positive *x* corresponds to positive values in Figures 2a, 2d, 2g, 2j, and 2m) and the NLIW velocity (red dots, colored by their log-scale energy) are shown in a polar plot. The along-shore and cross-shore coordinates are marked by black arrows; (b) a SAR image taken by Radarsat-2 on 16 July 2011, 02:09:21 UTC over the shaded area in Figure 1a with a zoomed-in plot, capturing a wave train passing by *ChaBa* (yellow star); (c) cross-shelf bathymetry of the area following the glider line in a); (d) time series of temperature and velocity in wave coordinates from *ChaBa* for the wave train detected in Figure 1b. Calculated maximum isotherm displacements are plotted in black lines. Black vertical dashed lines indicate wave troughs. Values of wave amplitude $\eta_w$, propagation direction $\theta_w$ and the standard deviation of calculated $\theta_w$ are marked. The red-dashed line indicates the time when the SAR image in Figure 1b was taken.

NLIWs are capable of transporting mass through Stokes drift and/or trapped cores, potentially contributing to cross-shelf exchange [*Huthnance*, 1995]. *Shroyer et al.* [2010b] reported that the onshore transport by NLIWs over a short period of time on the New Jersey shelf was comparable to a weak downwelling wind sustained over a much longer time, as also found on the Malin Shelf [*Inall et al.*, 2001]. An extreme case of NLIW mass transport is a trapped core, wherein waves trap water and carry it appreciable distances [*Lamb*, 2002; *Lien et al.*, 2012]. Plankton accumulation and transport in propagating nonlinear internal fronts have been reported and explored [e.g., *Pineda*, 1999; *Scotti and Pineda*, 2004], as well as sediment resuspension and transport of bottom material [*Bogucki et al.*, 1997; *Klymak and Moum*, 2003].

The Washington (WA) continental shelf (Figure 1a) is a highly productive, topographically complex region. Flow is generally dominated by a strong seasonal shelf current (southward in summer and northwestward in winter), primarily driven by winds that shift direction from northwesterly (upwelling-favorable) in summer to southerly (downwelling-favorable) in winter [*Hickey*, 1989; *Hickey and Banas*, 2003]. Seasonally averaged chlorophyll concentrations on the WA coast are several times higher than off northern California, where the

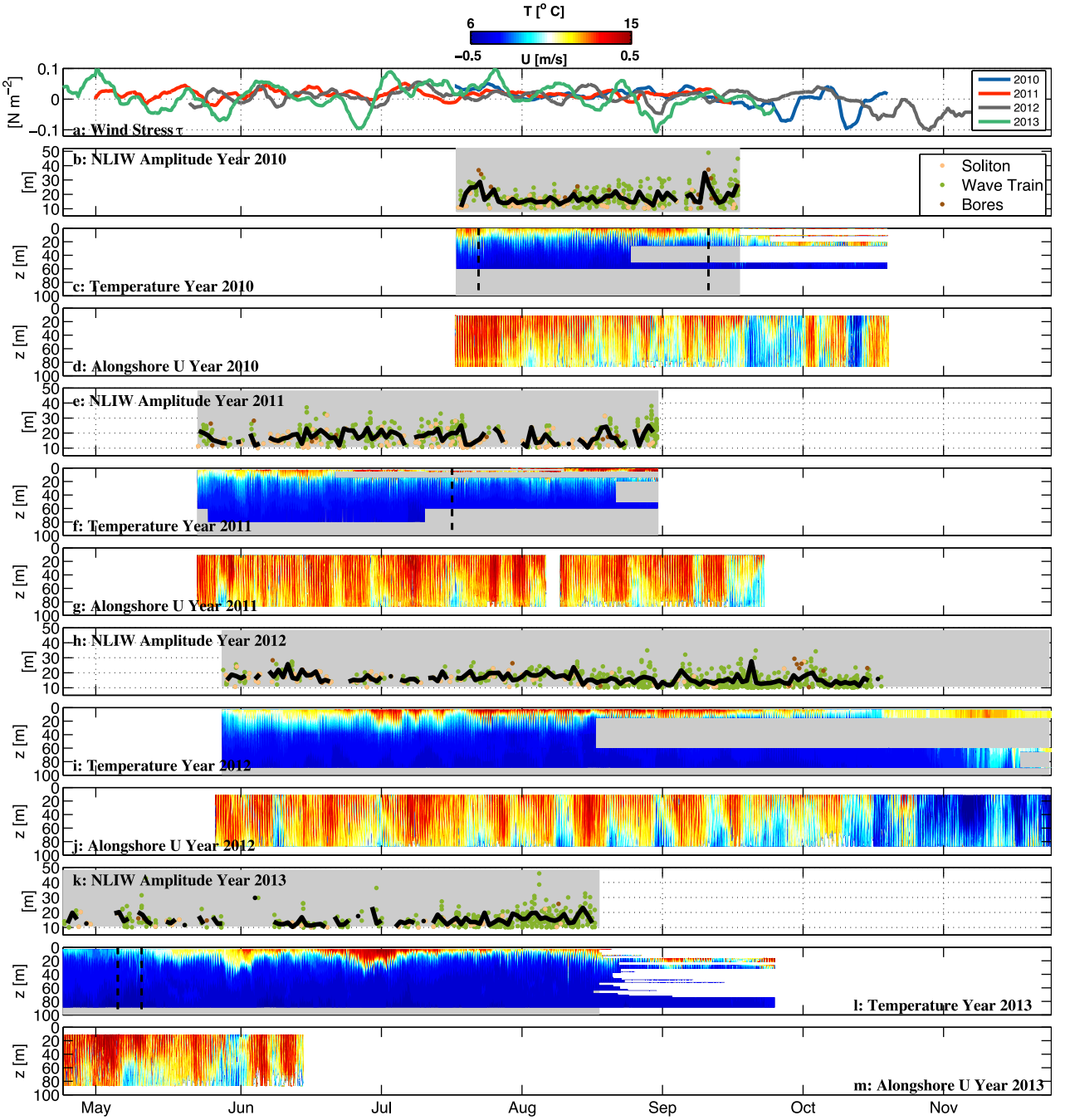


**Figure 2.** Data and nonlinear internal wave summary, showing (a) wind stress for all 4 years; (b) NLIW amplitude, colored by wave type (see text), and the running 1 day mean (black); (c) temperature; and (d) alongshore velocity measured at *ChaBa* in 2010. Positive values in Figures 2a and 2d correspond to positive *x* in Figure 1a. (e–g) As in Figures 2b and 2d but for 2011. (h–j) As in Figures 2b and 2d but for 2012. (k–m) As in Figures 2b and 2d but for 2013.

upwelling-favorable wind is several times greater [*Hickey and Banas*, 2008]. The high productivity off the WA coast remains a puzzle but possibly owes to (1) submarine canyons along continental slopes which can enhance upwelling [*Hickey*, 1995; *Waterhouse et al*., 2009; *Allen and Hickey*, 2010]; (2) a strong seasonal mesoscale feature known as the Juan de Fuca eddy [*MacFadyen et al*., 2008]; (3) the Juan de Fuca Strait; and (4) the Columbia river [*Stansfield et al*., 2001; *Hickey and Banas*, 2003]. These factors, individually or together, may catalyze nutrient supply to the euphotic zone. Most recently, strong NLIWs in this region are reported [*Alford et al*., 2012], potentially representing another important nutrient-supply mechanism. One example of a six-trough solitary wave train propagating onshore was captured by a high-resolution Synthetic Aperture

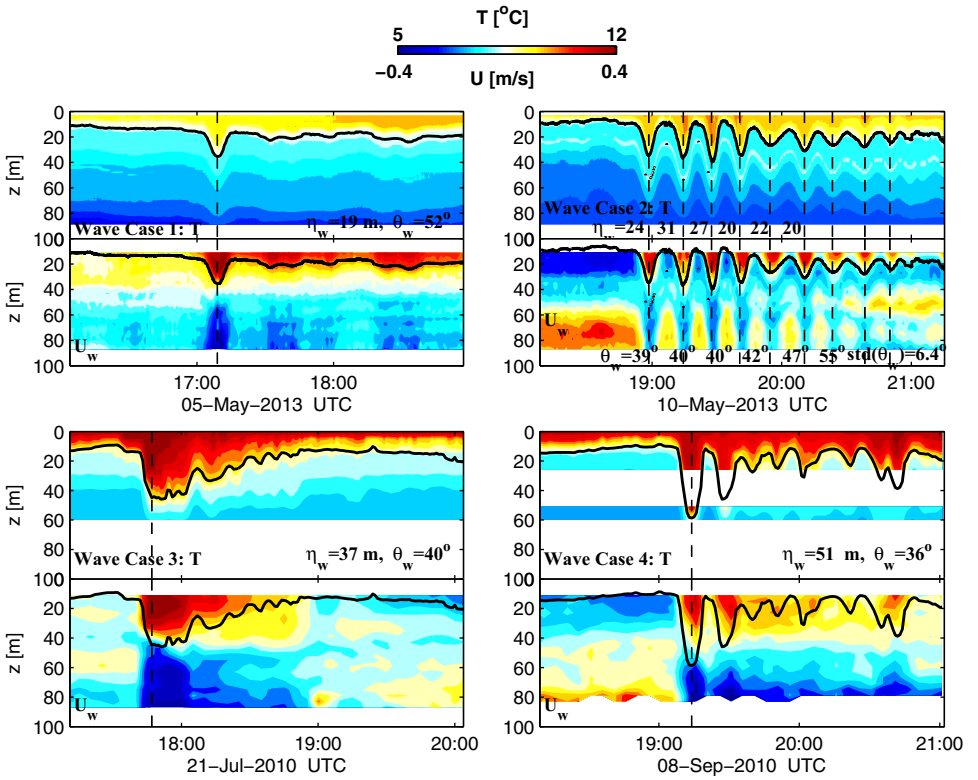


**Figure 3.** Four examples of NLIWs detected in the moored records, showing time series of temperature ($T$) and velocity along wave propagation directions ($U_w$) for a solitary internal wave (Case 1), a solitary wave train (Case 2), an internal bore (Case 3), and the largest wave in the record (Case 4). Vertical dashed lines indicate detected wave troughs. Maximum isotherm displacements are overplotted in black.

Radar (SAR) over this region on 16 July 2011, 02:09:21 UTC (Figure 1b). The same wave train was detected from surface mooring *"ChaBa"* (Figure 1d), deployed in 100 m deep water off the WA coast. Based on the mooring record, the wave train has a total of 6 solitary waves, with a largest wave of 28 m and a mean propagation direction toward ∼55° True (details in Section 2.), consistent with the SAR image.

In this study, four summer/fall time series of data from the *"ChaBa"* mooring are used to document > 1500 observed waves (Figure 2), and the background conditions that affect them. A distinct advantage of this data set is that a variety of wave types (Figure 3) and background conditions are captured in the long time series. Therefore, the temporal variations and potential relationships between NLIWs and background currents, stratification and the internal tide can be investigated. One limitation of this data set, however, is errors arising from nonideal vertical and temporal sampling. These are carefully examined in the analysis. The goals of this study are to 1) document the highly variable morphologies and properties of the NLIWs (amplitude, velocity, propagation direction, energetics and seasonal features); 2) obtain clues to their generation mechanism by examining their relationship with background conditions and the internal tide; and 3) estimate the onshore mass transport due to the waves and its possible implications.

This paper is organized as follows. The experimental setup, data and techniques are presented in section 2, including calculations of wave properties and errors associated with sampling using the dataset. Main results are presented in section 3, including the oceanographic context (section 3.1), basic wave features and their statistics (section 3.2), their relationship with the internal tide (section 3.3), and their on-shore transport (section 3.4), followed by a discussion in section 4 and conclusions in section 5.

## 2. Experimental Details

### 2.1. Data

Observations are from the *"ChaBa"* surface mooring and Seaglider *SG187*, both maintained by University of Washington as aspects of the Northwest Association of Networked Ocean Observing Systems (NANOOS).

*ChaBa* (47°58.0′N, 124°57.0′W) was deployed for four successive summers/falls (17 July to 17 October 2010, 22 May to 29 August 2011, 27 May to 20 November 2012, and 21 April to 23 September 2013) in 100 m deep water about 25 km off La Push, WA (Figures 1 and 2). *ChaBa* consists of a surface buoy housing meteorological instruments and communication, a subsurface instrument cage, and a string of instruments mounted along an 81 m mooring wire. A 230 kg depressor weight keeps the wire vertical, while a length of chain below keeps the instruments within a 60 m watch radius of the anchor on the seafloor. Data used in this study mainly include temperature and salinity measurements from conductivity-temperature-depth (CTD) sensors and velocity records from an acoustic Doppler current profiler (ADCP) mounted in the subsurface cage. During 2010–2012, temperature was measured at depths 0.5, 5, 11, 15, 20, 26, 40, 51, 60 m and 80 m (Figures 2c, 2f, and 2i; no 80 m sensor in 2010) with Seabird Electronics (SBE) 37 MicroCAT CTDs and SBE 39 T-loggers. Salinity was measured at depths 0.5, 11, 26 and 51 m by SBE 37s. The SBE 39s sampled every minute and the SBE 37s sampled every 2 min. In 2013, 40 SBE 56 T-loggers spaced over a 2 m interval between the surface and 80 m depth were added to the mooring, sampling temperature every 3 s over the battery lifespan (Figure 2l). A downward-looking 300 kHz Workhorse ADCP at 3 m depth recorded near-full-depth velocity profiles every 5 min in 2010–2012 (Figures 2d, 2g, and 2j), and every 1 min in 2013 (Figure 2m) over a 2 month period. Wind measurements are from National Data Buoy Center (NDBC) Station 46041 at Cape Elizabeth, located at 47°21.0′N, 124°42.5′W, about 60 km away from *ChaBa* to the southeast (Figures 1a and 2a). Other oceanic and meteorological properties, e.g., oxygen, nitrate, chlorophyll, pH, $pCO_2$ were sampled on the mooring wire or from the surface buoy, but are not discussed in this paper. Near-full-depth profiles of temperature and salinity complementing the vertically discrete *ChaBa* data are from Seaglider *SG187*, which ran across the WA continental slope/shelf between 47° N, 127° W and 48° N, 125° W (Figures 1a and 1c) during 2010–2012, giving a profile every 4–9 h, depending on water depth.

### 2.2. Methods

Time series of temperature ($T$) and alongshore velocity ($U$) over the full deployment in 2010–2013 (Figure 2) illustrate a marked semidiurnal internal tide, along with large spikes indicating nonlinear internal waves in their zoom-in plots (Figure 3). In this section, we document techniques used to calculate the wave properties and discuss potential errors due to sampling.

#### 2.2.1. Baroclinic Velocities

Because surface-wave-induced mooring motion is essentially vertically uniform, it contaminates the depth-averaged measured velocity $\mathbf{u}_{BT}$ but not the baroclinic velocity $\mathbf{u}_{BC}$ on time scales of seconds to minutes. Profiles of total velocity are constructed by first removing the depth-mean, time averaging the depth-mean over a three-point median filter to remove the mooring motion, and then adding it back to the depth-varying values. We define the baroclinic velocities as $\mathbf{u}_{BC}=\mathbf{u}-\mathbf{u}_{BT}$, where $\mathbf{u}_{BT}$ is the corrected depth-average flow, and $\mathbf{u}$ is corrected total velocity. $\mathbf{u}_{BC}$ is not affected by mooring motion.

#### 2.2.2. Estimation of Stratification $N^2$

Measurements of salinity ($S$) from SBE 37s on the mooring are sampled every 2 min and with a lower vertical resolution than $T$. Values of $S$ at depths where only $T$ is measured are estimated from a slowly varying $T$-$S$ relationship, using a linear piece-wise $T$-$S$ fit from the mooring data or glider data when available. Details of the $T$-$S$ fit and calculation of the stratification profile $N^2(z)$, where $N=\sqrt{\frac{g}{\rho}\frac{\partial\rho}{\partial z}}$ is the buoyancy frequency, $g$ is gravitation acceleration, $\rho$ is potential density, are described in Appendix A.

#### 2.2.3. Semidiurnal Tide Quantities

Semidiurnal barotropic and baroclinic tides are extracted from the moored records via bandpass filtering. The internal tide velocity, vertical displacement, energy, energy flux and their modal decompositions are calculated following standard procedures [e.g., *Alford and Zhao*, 2007]. Mode-1 internal tides are obtained from the filtered time series by performing a least square inverse.

#### 2.2.4. Calculation of NLIW Properties

##### 2.2.4.1. Amplitude

Wave amplitude $\eta_w$ is defined as the maximum isotherm displacement inside the wave event, i.e., $\eta_w=\eta(z,t_w)|_{max}$, where $\eta(z,t_w)=z(t_0)-z(t_w), z(t_w), z(t_0)$ are the isotherm depth at the time of maximum wave displacement and in the reference state, respectively. An example of the calculation of $\eta(z)$ is illustrated in Figure 4, where $\eta(z,t_w)$ is calculated as the vertical distance between the temperature profiles inside the wave ($T(z,t_w)$) and the reference state ($T(z,t_0)$). The difficulty in the designation of the reference state $t_0$ has been described in

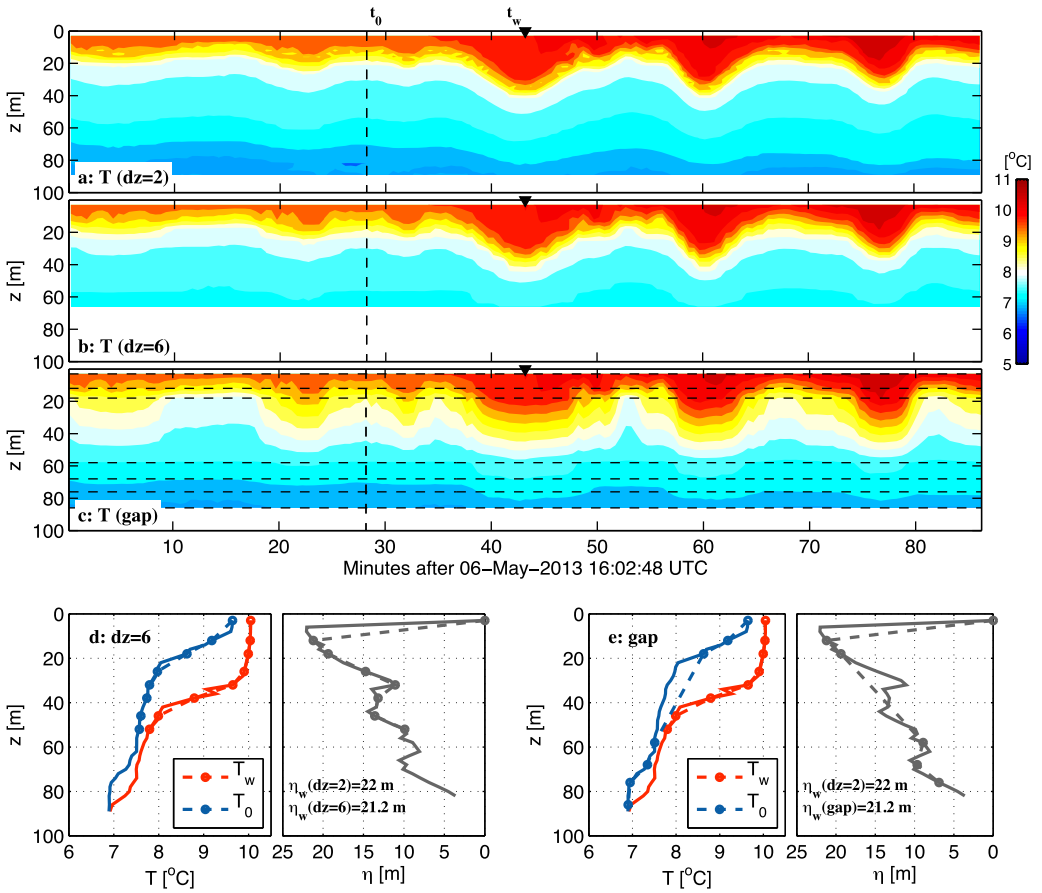


**Figure 4.** (top) Temperature time series for a wave detected in Year 2013, showing three cases: (a) the original sampling with a vertical spacing of $dz = 2$ m; (b) subsampled with $dz = 6$ m; and (c) subsampled with a gap in the midwater column. Vertical dashed lines in Figure 4c are depths of measurements. (d) Temperature profiles within the wave ($T_w$, red) and in the reference state ($T_0$, blue), and the corresponding isotherm displacements ($\eta(z, t_w)$, gray) calculated in the subsampled case of $dz = 6$ (dashed) compared to the full-resolution data (solid). (e) As in Figure 4d but for the subsampled case with a gap.

*Shroyer et al.* [2010a]. We define $t_0$ to be 15 min before the maximum wave displacements. $\eta_w$ is defined positive for depression waves, as no elevation waves are detected. Perturbations with $\eta_w > 10$ m are classified as NLIWs.

#### 2.2.4.2. Velocity and Direction

The horizontal wave velocity vector in Earth coordinates ($\mathbf{u}_w = (u_w, v_w)$) is calculated as velocity measurements in the wave event minus the background flow [*Chang et al.*, 2011], i.e., $\mathbf{u}_w(z) = \mathbf{u}(z, t_w) - \mathbf{u}(z - \eta(z), t_0)$, in which $\mathbf{u}(z, t_w)$ and $\mathbf{u}(z - \eta(z), t_0)$ are the measured velocities inside the wave and their background states along isopycnals, respectively. $t_0$ is again defined as 15 min before the wave arrival. Mode-1 depression waves have opposing deep/shallow flows, such that the wave propagation direction $\theta_w$ is consistent with the direction of the shallow flow. Therefore $\theta_w$ is calculated as $tan^{-1}\frac{v_w(z)}{u_w(z)}$ in the shallow flow following *Chang et al.* [2011], using the fitted slope of $v_w$ over $u_w$. The horizontal wave velocities in wave coordinates ($U_w$, $V_w$) are calculated by rotating $u_w$, $v_w$ toward the wave propagation direction. Because the motion of the surface buoy renders vertical motions unusable [*Alford et al.*, 2012], the vertical wave velocity $W_w$ is estimated by $\frac{\Delta\eta(z)}{\Delta t}$, which is usually an order of magnitude smaller than the horizontal velocities, similar to other observational studies [e.g., *Moum et al.*, 2003; *Lien et al.*, 2013].

Errors in $\theta_w$ are estimated by comparing $\theta_w$ within the same wave train, under the assumption that waves within a train propagate in the same direction. Wave trains consisting of three or more waves are used in this analysis and $\theta_w$ usually has a standard deviation of $\sim 8^\circ$ (e.g., Figures 1 and 3, Case 2), with a maximum difference of $\sim 20^\circ$ between the waves.

#### 2.2.4.3. Phase Speed

For energy flux, we require knowledge of the phase speed $c$, as the phase speed equals the group speed for nondispersive waves. We do not have direct observations of $c$, and mooring motion precludes calculation

of $c$ from the lateral separation of the ADCP beams following *Scotti et al*. [2005]. Instead, $c$ is estimated from the Dubreil-Jacotin-Long (DJL) model [*Long*, 1953; *Stastna and Lamb*, 2002], i.e.,

$$\nabla^2\eta+\frac{\partial_z\bar{U}(z-\eta)}{c_{\mathrm{DJL}}-\bar{U}(z-\eta)}[\partial_x^2\eta+(1-\partial_z^2\eta)^2-1]+\frac{\bar{N}^2(z-\eta)}{[c_{\mathrm{DJL}}-\bar{U}(z-\eta)]}\eta=0 \tag{1}$$

where $\eta$ is the displacement, $\nabla^2=(\partial_x^2+\partial_z^2)$ ($x$, $z$ is the horizontal and vertical direction in wave coordinates), $\bar{U}$ and $\bar{N}$ are the background velocity and stratification, respectively, and $c_{\mathrm{DJL}}$ is the calculated phase speed. Because it is fully nonlinear and nonhydrostatic, the DJL model is a decent simulation of these waves in terms of wave shape and phase speed, and is applicable for steady waves of all amplitudes [*Stastna and Lamb*, 2002; *Henyey*, 1999; *Lamb*, 2003; *Lien et al*., 2012]. The steady approximation is a good one at our site considering the relatively flat bottom. Previous observational studies suggest that $c_{\mathrm{DJL}}$ is typically within 10% of the observed $c$ [*Lien et al*., 2012]. This error in our estimation of phase speed is projected onto the wave energy, energy flux and transport calculations, which are discussed later in this paper.

#### 2.2.4.4. Wave Duration and Width

The wave duration time $\tau_w$ is defined as that between the start and end of a wave event, i.e., between the times when the isopycnal displacement is greater than 2% of the maximum isotherm displacements before and after wave arrivals. Wave width at half amplitude $\lambda_{1/2}$ is that between the half downwelling and upwelling displacement, estimated from time series with the assumption that $c=c_{\mathrm{DJL}}$, which introduces about 10% error into the calculation.

#### 2.2.4.5. Energetics

The wave energy is the sum of available potential energy and kinetic energy. Available potential energy density $E_a(z)$ (units: $\mathrm{Jm}^{-3}$) is calculated following *Scotti et al*. [2006] and *Lamb* [2007], as

$$E_a(z)=g\int_{\bar{\rho}(z)}^{\rho(z)}[z-z_0'(s)]ds \tag{2}$$

in which $\rho(z)$, $\bar{\rho}(z)$ are the density profiles inside the wave and in the reference state, respectively; $z'_0(s)$ satisfies $\bar{\rho}(z'_0(s))=s$ for a monotonic reference density profile $\bar{\rho}(z)$. So defined, APE is the total energy required to restore isopycnals to the upstream reference state [*Holliday and McIntyre*, 1981], and is consistent with *Moum et al*. [2007b] and *Shroyer et al*. [2010a] when integrated over the entire domain used to calculate the reference state [*Winters and Barkan*, 2013]. *Kang and Fringer* [2010] discussed three definitions of APE in the context of NLIWs and concluded that (2) is the preferred one, since use of (2) introduces the smallest errors when computing the energy conservation laws.

The kinetic energy density $E_k(z)$ is defined as $E_k=u_w^2+v_w^2+w_w^2$. Since the vertical velocity $w_w$ is usually an order of magnitude smaller than the horizontal velocities, and we do not directly measure it, the horizontal kinetic energy density $E_{hk}$ is used to approximate $E_k$. $E_{hk}$ is calculated as $E_{hk}=\frac{1}{2}\rho_0(\overline{\mathbf{U}}^2+\mathbf{U}_w^2+2*\overline{\mathbf{U}}\times\mathbf{U}_w)$ following *Lamb* [2010], where $\mathbf{U}_w$ and $\overline{\mathbf{U}}$ are the horizontal wave velocity and background velocity in wave coordinates. With this formulation, the presence of a sheared background current may introduce important consequences for the evolution of the mechanical energy in the system [*Lamb*, 2010].

Integrating $E_a$ over depth and the horizontal extent for each individual wave, wave available potential energy $E_{\mathrm{A}}$ (units: $\mathrm{Jm}^{-1}$) is calculated as $E_{\mathrm{A}}=\int\int cE_a(z)dzdt$. A constant wave propagation speed of $c_{\mathrm{DJL}}$ is assumed here, which introduces $\approx$ 10% error into the wave energy calculation. Similarly, wave kinetic energy $E_{\mathrm{K}}$ and total energy $E_w$ are calculated for each wave in the data set.

### 2.2.5. Sampling Errors

The spatial and temporal resolution of the temperature and velocity sampling in 2010, 2011, and 2012 are not ideal for nonlinear internal wave detection. The vertically discrete CTD measurements and the 5 min sampling of ADCP in 2010–2012 impact the calculation of wave properties. In 2013, we substantially improved the vertical resolution of the temperature measurements (2 m) and the sampling frequency of both temperature and velocity (3 sec and 1 min, respectively). Temperature records in 2013 are used to estimate the impacts of vertically discrete measurements and gaps over the water column on the calculation of $\eta_w$ and $E_A$ in 2010–2012. Velocity records in 2013, sampled every 1 min, are subsampled each 5 min to examine the effects of the temporal resolution of velocity data in 2010–2012 on $U_w$ and $E_{\mathrm{HK}}$. These effects are discussed below.

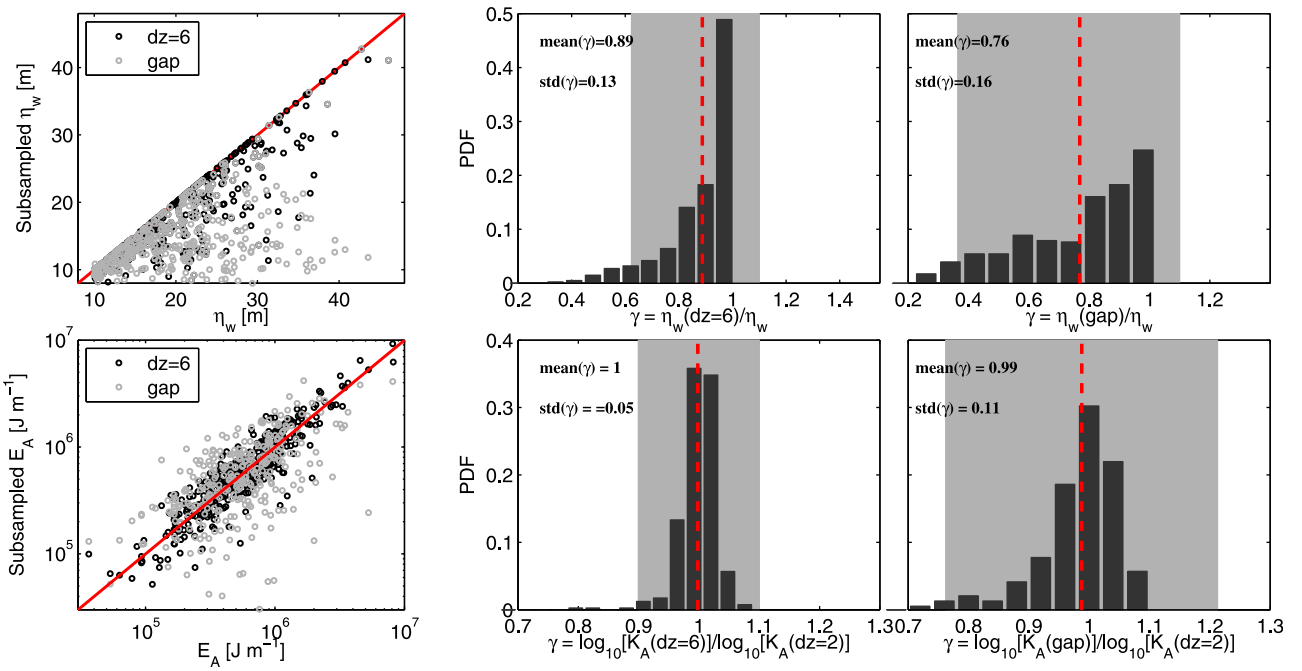


**Figure 5.** (top) Examination of the sampling effects on $\eta_w$ estimation, including (left) a scatter plot showing the subsample cases and the original data for $\eta_w$ analysis and (middle) PDF plots showing the ratio between $\eta_w$ calculated from two subsample cases: $dz = 6$ and (right) a gap in the midwater column. (bottom) Same analysis but for $E_A$ estimation. Red-dashed lines indicate sample means. Gray indicates theoretical 95% confidence intervals.

Temperature data in 2010–2012 have variable vertical spacing and gaps (Figure 2), which generally fall into three categories: (1) discrete temperature measurements over the water column at a vertical spacing of $dz = 6$ m, which represents most of the periods when sensors were functioning (e.g., June–July, Figures 2c, 2f, and 2i); (2) a gap in temperature measurements between a depth of 15 m and 60 m, which represents a significant portion of the data in Year 2012 after a sensor stopped functioning (e.g., September, Figure 2i); (3) a gap extending to the surface (e.g., late September 2010 to October 2010, Figure 2c). The effects of 6 m-spaced $T$ measurements (Category 1) on the estimation of $\eta_w$ and $E_A$ are small (Figures 4b and 5). When gaps occur over the middle water column (Category 2), $\eta_w$ is underestimated by an average of 24% and the $E_A$ estimation is considerably scattered (Figures 4c and 5). When gaps are close to the surface (Category 3), the NLIW detection is unreliable due to their surface-intensified structures (not shown) and these records are removed in the analysis. Gray regions in Figure 2 indicate periods when coverage was adequate for reliable wave detection (Category 1, 2).

The 5 min velocity data in 2010–2012 are marginal for waves with typical duration of 10–20 min, therefore affecting the wave velocity and kinetic energy. An example of a wave train consisting of three waves observed on 6 May 2013 (Figure 6) suggests that the 5 min subsampling captures the waves, but tends to under-estimate the wave velocity depending on the sampling time. The maximum wave velocity $U_{max}$ is underestimated by an average of 14%, and the wave horizontal kinetic energy $E_{HK}$ estimation is scattered with a standard deviation of 32% (Figure 7). These errors propagate into the energy flux and transport calculations, which are discussed later in Section 3.

## 3. Results

### 3.1. Oceanographic Context

Washington's continental shelf has a strong seasonal wind-driven current. In spring/summer, winds are predominantly northerly (Figure 2a) and drive a southward shelf current (Figures 2d, 2g, 2j, 2m, and 8d, black lines). In fall/winter, winds are predominantly southerly, resulting in a northward shelf current and effectively reversing the cross-shelf circulation pattern (Figures 2d, 2g, 2j, 2m, and 8d, gray lines). As a consequence of this and presumably increased wind mixing as fall storms set in, there is a clear distinction in the

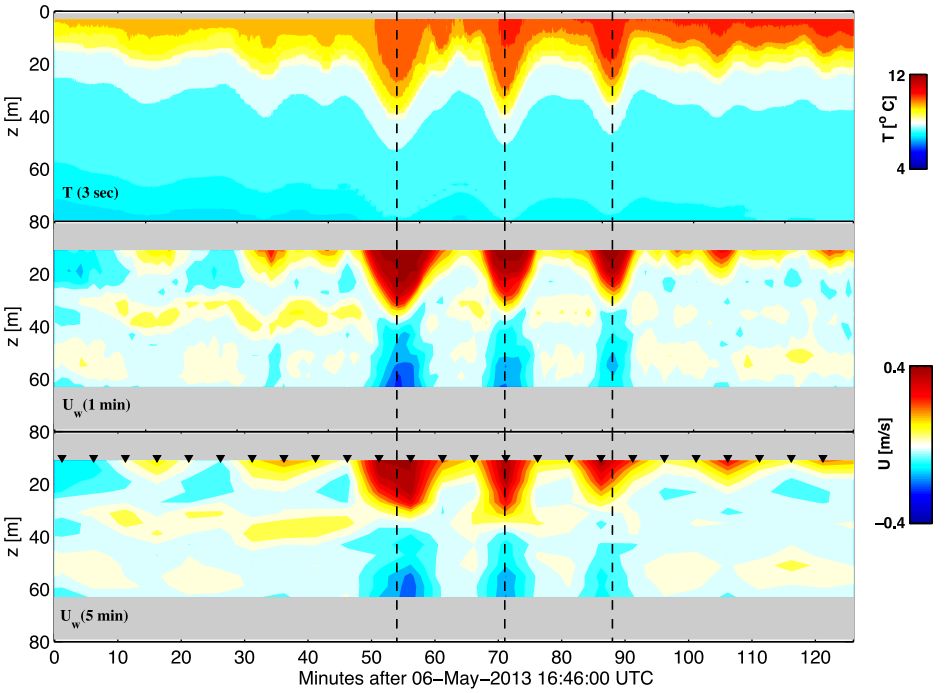


**Figure 6.** Temperature, 1 min velocity and subsampled 5 min velocity for a wave detected on 6 May 2013. Vertical dashed lines denote detected wave troughs. Black triangles denote the 5 min subsampling time.

stratification between upwelling and downwelling seasons (Figures 8a–8c). In spring and summer, stratification is concentrated near the surface, with weaker stratification and a deeper thermocline seen in winter. Event-scale (3–7 days) wind reversals (southerly winds) primarily caused by storms are commonly observed (Figure 2a, filled areas), which are typically weaker in spring/summer and stronger in fall. During storms, currents often reverse and mixed layer depth increases.

### 3.2. Wave Properties

Time series of wave amplitude $\eta_w$ in all four years (Figures 2b, 2e, 2h, and 2k) suggest that waves are present much of the time. A weak seasonal pattern is suggested in that $\eta_w$ remains generally smaller in spring and early summer (with most waves showing $\eta_w < 30$m), increasing near the end of August and September (with more occurrence of $\eta_w > 30$m). In the record of 2012, the only year when the mooring remained in the water until December, no NLIWs are detected after 15 October (Figure 2h), likely due to the greatly reduced stratification. Storms also appear to impact the presence of waves (e.g., 15 May, 1 June, and 29

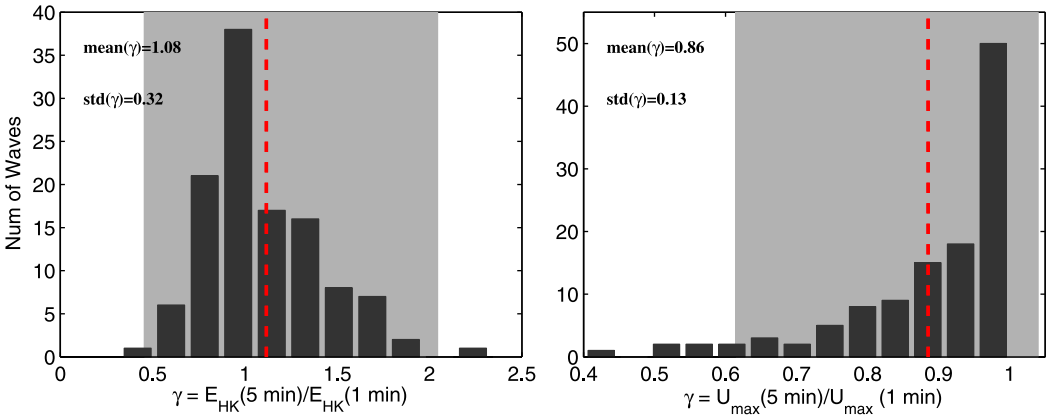


**Figure 7.** PDF plots of the ratio between 5 min subsample velocity data and the original velocity data, for (left) calculated wave kinetic energy $E_{HK}$ and (right) the maximum wave velocity $U_{max}$. Red-dashed lines indicate sample means. Gray indicates theoretical 95% confidence intervals.

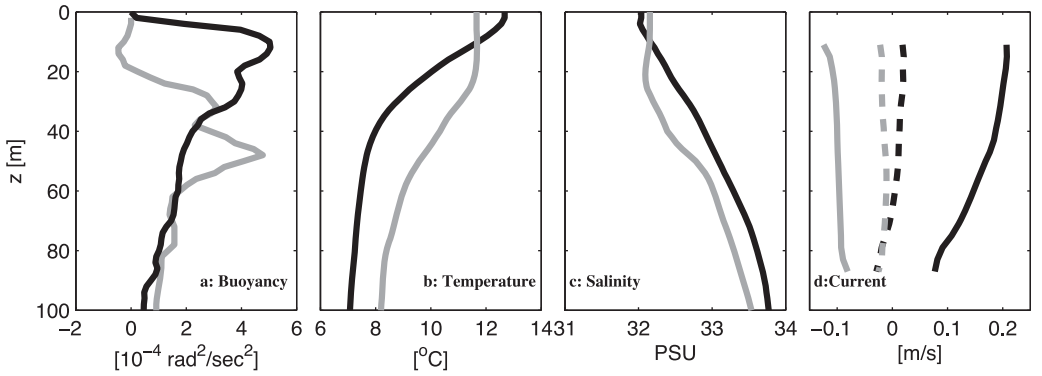


**Figure 8.** Profiles of (a) background stratification $N^2$, (b) temperature, and (c) salinity from the glider. (d) Background along-shore (solid) and cross-shore (dashed) currents in spring/summer (black) and fall/winter (gray) from the mooring.

June in 2013), when the number of detectable NLIWs significantly decreased. However, these factors do not explain why there are more and stronger waves in some periods (e.g., 14–19 September 2010; 16–24 June 2011), with fewer and weaker waves in some other periods (e.g., 26–30 July 2011; 16–22 June 2012). Instead, NLIW occurrence is correlated with the internal tide energy flux, as we will demonstrate in Section 3.3.

Detected wave amplitude $\eta_w$ has most common values of 10–20 m (Figure 9a), with an average of 15 m and a maximum of 52 m (Figure 3, Case 4). The percentage of waves with amplitude greater than 40 m (30 m) is 0.4% (3.7%), out of a total of 1533 waves. The DJL phase speed $c_{DJL}$ mostly falls between 0.4 and 0.6m $s^{-1}$ (Figure 9b), typical for internal waves on shelves. Wave width at half amplitude $\lambda_{1/2}$, defined as the distance over which the amplitude decreased by half, assuming $c=c_{DJL}$, is mostly between 100 and 300 m, with a mean of 260 m (Figure 9c). A small percentage of waves have $\lambda_{1/2}$ extending to 500 m or even 1000 m (Figure 9c), which correspond to the long-lived internal bores.

Wave energy $E_w$ displays a considerable range from $10^4$ to $10^8$ $Jm^{-1}$, with a typical magnitude of 1 $MJm^{-1}$ (Figure 9d). The ratio between $E_A$ and $E_K$ falls close to the line of 1:1, which is expected for stable waves, but displays an order of magnitude scatter (Figures 9e and 9f). Part of the reason for this scatter is due to our limited sampling as discussed earlier. Another possible source of error is associated with the estimation of the reference state, for both $E_A$ and $E_K$ calculation, particularly when wave signals are weak compared to background signals. With these errors in consideration, the fact that $E_A$ is higher on average than $E_K$ by fraction of ~20% agrees with studies by *Lamb and Nguyen* [2009], *Moum et al*. [2007b], *Shroyer et al*. [2010a], and *Lien et al*. [2013], indicating the potential of shoaling waves or the effect of spatial variations in the background current [*Lamb*, 2003, 2010].

Wave propagation direction $\theta_w$ is primarily toward the northeast (Figure 1a, red dots), with a most common value of 50°T. Most scatter in $\theta_w$ is due to weaker waves, while the most energetic waves propagate toward the northeast or north-northeast almost exclusively. The similarity of $\theta_w$ to the direction of internal tide energy flux (Figure 1a, red arrow), suggests that the two may have the same energy source [*Alford et al*., 2012]. NLIW are directed slightly more toward the east than the internal tide due to the depth dependence of the wave speed, which could be explained by bathymetric refraction and the smaller wave speed of the internal tide compared to NLIWs. That is, the phase speed of internal waves decreases as water depth decreases, such that their wave crests continuously adjust to follow the isobaths (Figure 1b), making the nonlinear internal waves propagate more toward the east than the internal tide.

All 1533 detected waves are mode-1 waves of depression, but have very different forms, which we loosely group into three categories based on the wave width $\lambda_{1/2}$. Waves are categorized as internal solitary waves (ISW, $\lambda_{1/2} < 500$ m), solitary wave trains (including more than one ISW) or internal bores ($\lambda_{1/2} > 500$ m). Examples of a single internal solitary wave, a solitary wave train, and an internal bore are given by Case 1, Case 2 and 4, and Case 3 in Figure 3, respectively. Internal bores account for 8.5% of the observed NLIWs, with the rest being ISWs in a train (~74%) or alone (~18%).

The occurrence of each wave type is not yet predictable (Figure 2), although more bores tend to be observed in September and October while solitary waves are more common in spring (e.g., Figure 2, Year 2010, 2012). The complexity of wave taxonomy is not surprising in a topographically complicated coastal

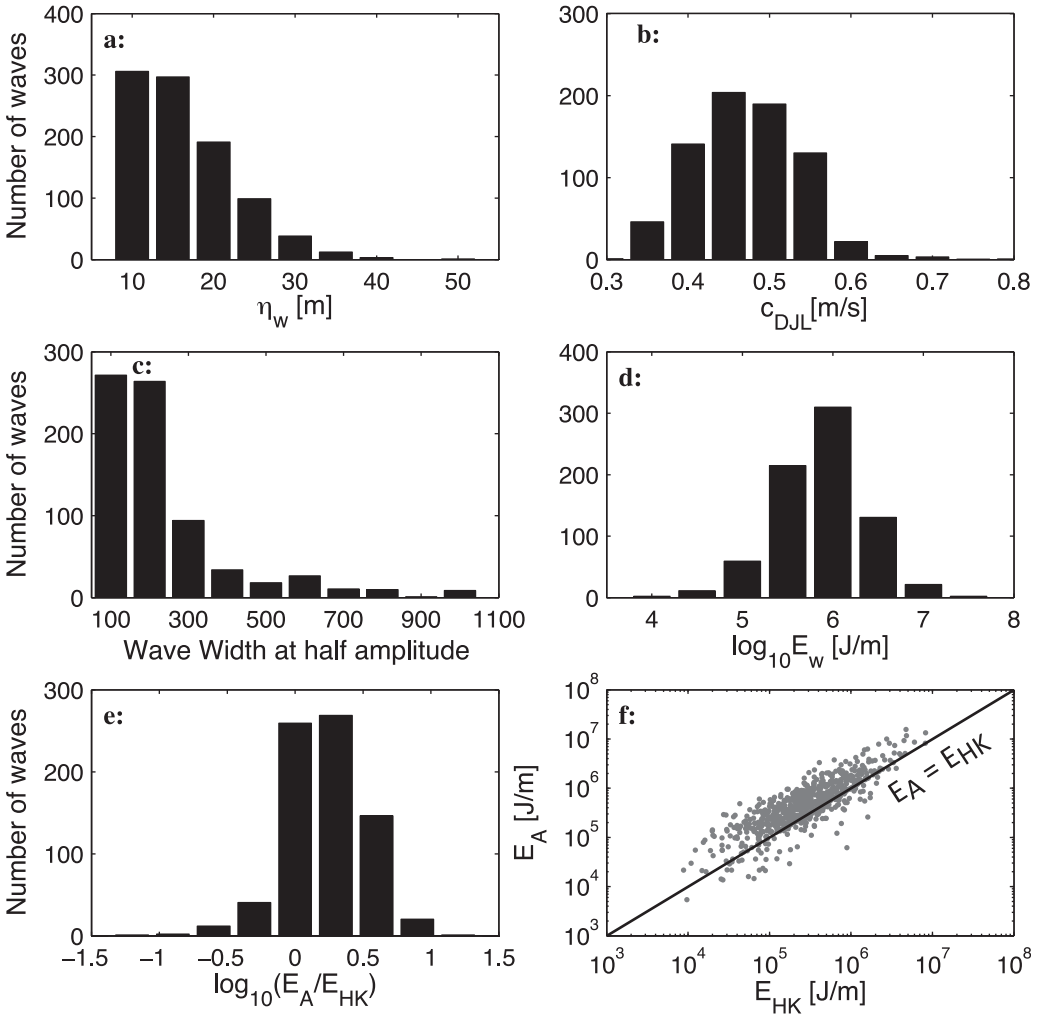


**Figure 9.** Histograms of basic features of NLIWs detected in 2010, 2011, and 2012, including (a) wave amplitude $\eta_w$, (b) DJL phase speed $c_{DJL}$, (c) wave width at half amplitude $\lambda_{1/2}$, (d) log-scale total energy $\log_{10}E_w$, (e) log-scale ratio of wave available potential energy $E_A$ over horizontal kinetic energy $E_{HK}$, and (f) a scatter plot of $E_A$ over $E_{HK}$, with 1:1 indicated by a black line.

region like the WA coast, and is presumably related to the complex generation/evolution process and the temporal and/or spatial variation in the background shear and stratification.

### 3.3. Relationship With the Internal Tide

As discussed earlier, NLIWs are primarily generated by (i) lee waves, or (ii) nonlinear transformation of the baroclinic tide as it propagates onshore. The hypothesis in this study is that NLIWs off the WA coast are primarily generated by mechanism ii), which is supported by the phase relationship between NLIWs and the internal/barotropic tide, as well as correlation between their energy fluxes.

Strong mode-1, semidiurnal internal tides exist in the record (e.g., Figure 10b), with typical downward phase propagation, indicating upward energy propagation. Mode-1 internal tide energy flux $F_{IT}$, calculated following *Alford* [2003], *Nash et al.* [2005], and *Alford and Zhao* [2007], is toward the north-northeast in all four years, with a mean of about 80Wm$^{-1}$ (Figure 1a). Because internal tide fluxes from a regional numerical model are substantially smaller, *Alford et al.* [2012] concluded that the internal tides have a remote source, possibly the Mendocino escarpment. Semidiurnal barotropic tidal currents in this region are about 0.2ms$^{-1}$, with ellipses oriented along-shelf [*Alford et al.*, 2012].

NLIWs generally arrive semidiurnally with the internal tide, usually at isotherm depressions (e.g., Figures 10a–10c). The phase relationship is examined by the arrival time of NLIWs relative to the zero-crossing of the tidal phase based on the internal tide velocity ($U_{bc}$), displacement ($\eta_{bc}$) and barotropic tide velocity

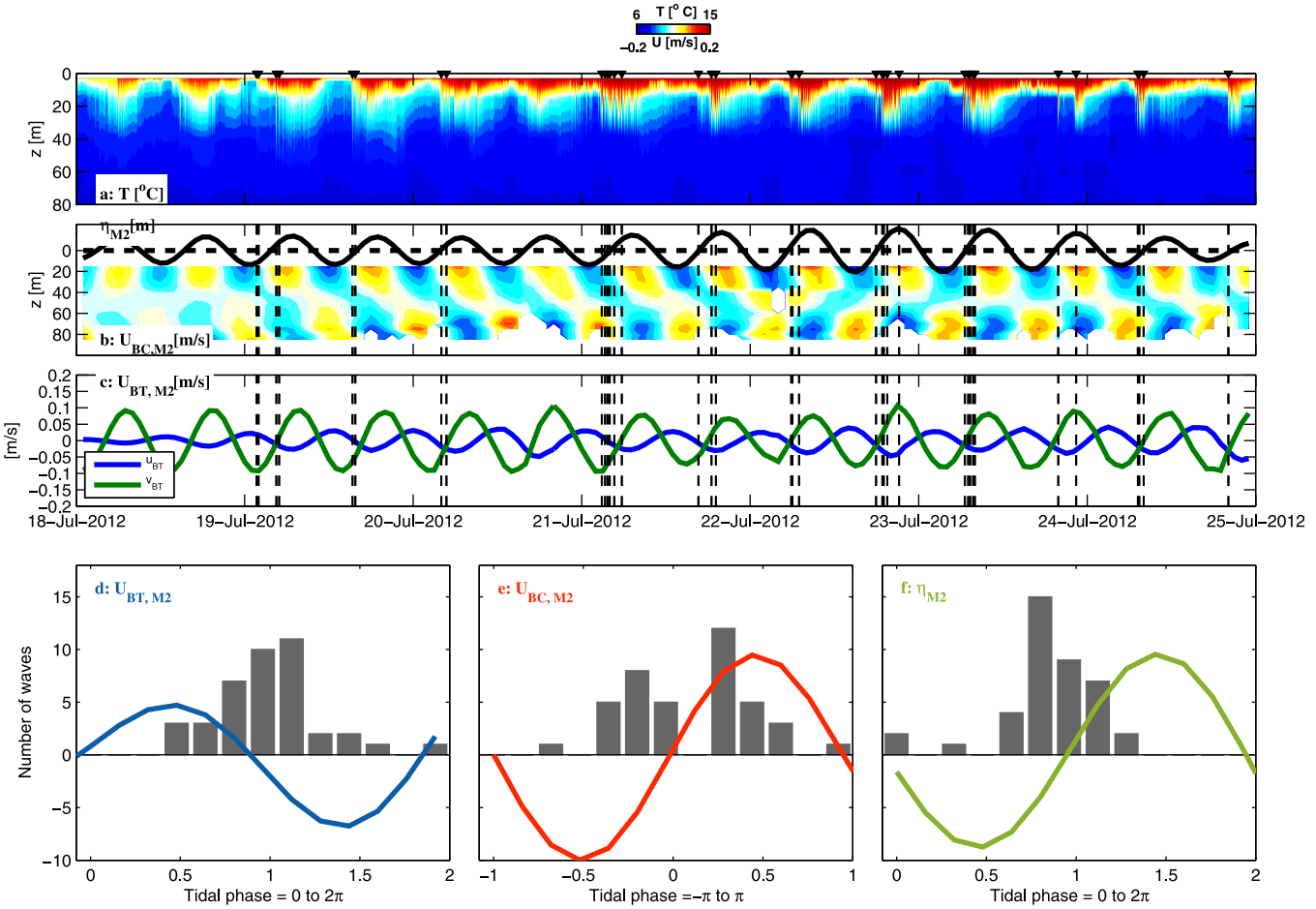


**Figure 10.** A 7 day period during 18–25 July 2012, showing (a) temperature, (b) semidiurnal baroclinic velocity in the wave propagation direction $U_{bc}$ and isopycnal displacement $\eta_{M2}$ at a depth of $z = 15$ m, and (c) semidiurnal barotropic velocities $U_{bt}$, $V_{bt}$. Wave arrival times are indicated by black triangles in Figure 10a and vertical dashed lines in Figures 10b and 10c, respectively. (d)–(f) Histograms of number of waves with arrival times relative to the tidal phase of $U_{bt}$, $U_{bc}$ and $\eta_{IT}$, respectively.

($U_{bt}$). Most NLIWs in this period arrive together with the internal tide at a phase lag between $-0.4\pi$ and $0.4\pi$ for $U_{bc}$ and between $0.4\pi$ and $1.4\pi$ for $\eta_{bc}$ (Figures 10e and 10f). Note that there is also a peak in the wave arrival time for the the barotropic tide (Figure 10d), most likely because the internal tide and the barotropic tide are phase-locked during this time. In other periods, the waves arrive fairly irregularly and without clear tidal modulation (not shown).

If NLIWs arise from the internal tide, then their energy fluxes should be correlated [*Nash et al.*, 2012]. Following *Moum et al.* [2007b], energy flux $f_E$ (units: $Wm^{-1}$) for each wave is calculated as:

$$f_E = c\langle E_z \rangle \tag{3}$$

in which $\langle E_z \rangle$ is the depth-integrated total energy density averaged over a wave length, and $c$ is approximated by $c_{DJL}$. Because the waves are episodic, $f_E$ is averaged over every 48 h window as

$$\langle f_E \rangle_{48h} = \tau_{w_i} f_{E_i} / 48\,h \tag{4}$$

in which $\tau_{w_i}, f_{E_i}$ are the duration and energy flux of the $i$-th NLIW, respectively. The average value of $\langle f_E \rangle$ (used as the short form of $\langle f_E \rangle_{48h}$ hereafter) is 144, 57, and 61 $Wm^{-1}$ in 2010, 2011, and 2012, respectively (2013 data are removed in this analysis due to their short velocity records). The magnitudes of $\langle f_E \rangle$ and $F_{IT}$ are similar, and generally weakly correlated (Figures 11a–11c). On the other hand, the local barotropic forcing $F_{BT}$ (Figure 11d), computed by $\langle N_B^2 u_{BT}^2 \rangle$ [*Baines*, 1974], where $N_B^2$ is the stratification within 40 m of the bottom, $u_{BT}$ is the barotropic tidal currents in the cross-shelf direction, is visually unrelated with $\langle f_E \rangle$. Note this measure of barotropic forcing is an approximation to the forcing at shelf break, and has a nonexistent, or at best irregular, spring/neap cycle, typical for coastal regions [*Nash et al.*, 2012].

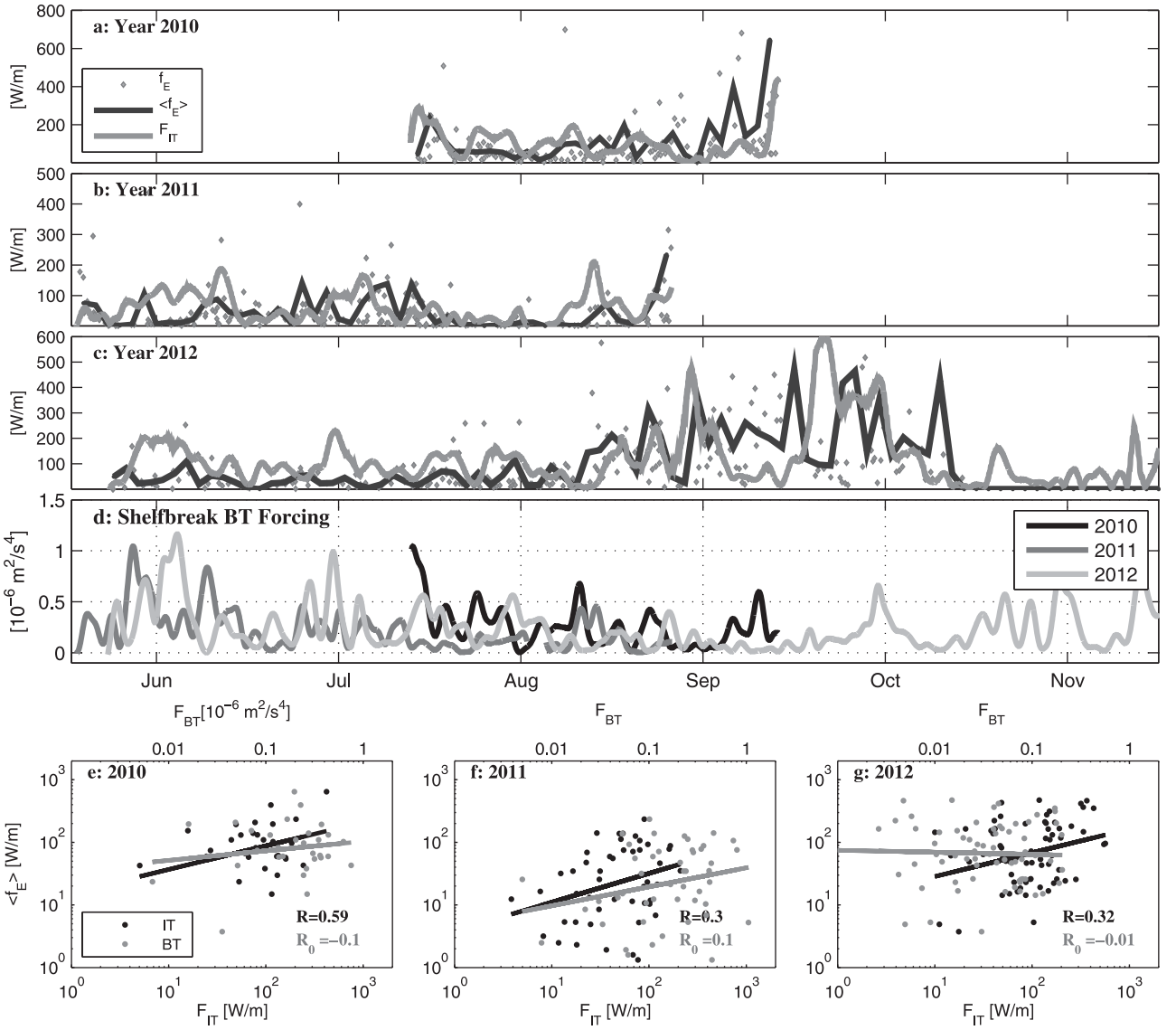


**Figure 11.** (a)–(c) Time series of 48 h averaged NLIW energy flux ($\langle f_E \rangle$, black lines), contribution to the energy flux from individual NLIW ($f_E$, gray dots), and mode-1 IT energy flux ($F_{IT}$, gray lines) in 2010, 2011, and 2012; (d) local barotropic forcing over the shelf break ($F_{BT}$); (e)–(g) scatter plots of $\langle f_E \rangle$ over $F_{IT}$ (black) and $F_{BT}$ (gray), with corresponding values of correlation coefficients $R$ and $R_0$ noted, for records in 2010, 2011, and 2012. Lines indicate the best linear fit in each case.

Calculated correlation coefficients $R$ between $\langle f_E \rangle$ and $F_{IT}$ are 0.59, 0.3 and 0.32 in 2010, 2011, and 2012, respectively, all of which are significant at a level of 95% based on $t$ test statistics. By contrast, correlation coefficients $R_0$ between $\langle f_E \rangle$ and $F_{BT}$, with values of −0.11, 0.1 and 0.01 in the three years, are not statistically significant. Note that $\langle f_E \rangle$ and $F_{IT}$ are not entirely independent since the NLIW signals, in particular internal bores, project onto the semidiurnal internal tide motions, as discussed in *Nash et al.* [2012]. The correlation between the flux magnitude, similar direction of NLIWs and the internal tide, and the lack of correlation with the barotropic tide suggest that NLIWs are formed when remote internal tide steepen as they propagate onshore, instead of by direct local conversion from the barotropic forcing. It is noted that the correlation between $\langle f_E \rangle$ and $F_{IT}$ are significant but not high, suggesting the importance of other factors such as bathymetry, background currents and shear.

### 3.4. Cross-Shore Transport

Nonlinear internal waves provide a mechanism for the transport of water mass over the continental shelf, making them a potentially important avenue for lateral movement of fluid, nutrients, larvae, and other biota as discussed earlier. *Huthnance* [1995] suggested that NLIWs may contribute significantly to cross-shore

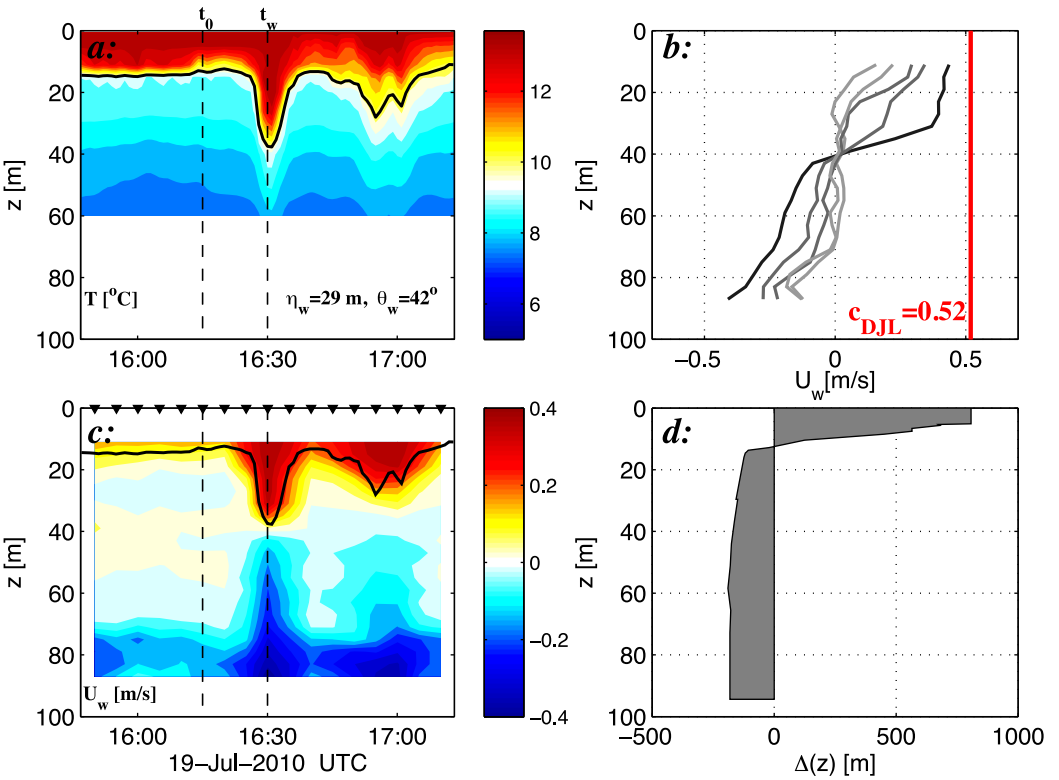


**Figure 12.** (left) Temperature and velocity for a wave detected on 19 July 2010. Maximum isotherm displacements are overplotted in black. Vertical dashed lines indicate the background state ($t_0$) and the wave trough ($t_w$). Black triangles indicate sampling times of velocity. (top right) Wave velocity profiles (colored by the isotherm displacements; black indicates the wave trough, i.e., maximum displacements) compared to the DJL phase speed $c_{DJL}$. The Stokes drift profile $\Delta(z)$ at the wave trough (lower right).

exchange in some locations, with a typical depth-integrated transport $\bar{U}_T \sim 1\mathrm{m}^2\mathrm{s}^{-1}$. This idea has been investigated using numerical models [*Lamb*, 1997] and observational tools [*Inall et al*., 2001; *Shroyer et al*., 2010b]. *Shroyer et al*. [2010b] found an average NLIW transport of $0.3\mathrm{m}^2\mathrm{s}^{-1}$ over New Jersey's shelf, similar to the observations by *Inall et al*. [2001] on the Malin Shelf. Following *Lamb* [1997], *Huthnance* [1995], and *Shroyer et al*. [2010b], vertically integrated transport due to NLIWs is calculated as

$$U_T = \int \Delta(z)/\tau(z)dz \tag{5}$$

where $\tau(z)$, approximated by the wave duration time, is the amount of time a parcel of water at a given equilibrium depth is advected by the wave; $\Delta(z)$ is the particle transport distance due to Stokes drift, defined as $\Delta(x,z) = \int_{x'_{\mathrm{start}}}^{x'_{\mathrm{end}}} \frac{U_w(x,z)}{c - U_w(x,z)} dx'$ following *Lamb* [1997] and *Shroyer et al*. [2010b] in wave coordinates. $U_w$ was calculated by subtracting the background velocity interpolated along isopycnals (assuming streamlines follow isopycnals) and evaluated along constant density surfaces to find $\Delta$ as a function of undisturbed depth (Figure 12d). Note that this expression does not to take into account the vertical motion of particles which is an order of magnitude smaller than the horizontal velocity. The calculation requires $U_w < c$ (as $c \to U_w, \Delta \to \infty$), which is valid for about 99% of the waves detected in our study. Integration of $\Delta(z)$ over the surface to the first zero-crossing point gives an estimate of $U_T$ and $\bar{U}_T$ is calculated as the average of $U_T$ for each wave. The daily averaged onshore transport is then calculated as $\langle \bar{U}_T \rangle = \sum_{i=1}^{n} \tau_{w_i} \bar{U}_{T_i} / 24h$, in which $n$ is the number of waves within the day, $\tau_{w_i}$ is the duration of the $i$-th wave. $\langle \bar{U}_T \rangle$ has a mean (median) of 0.48 (0.36), 0.16 (0.08) and 0.49 (0.28) $\mathrm{m}^2\mathrm{s}^{-1}$ in Year 2010, 2011, and 2012, respectively. Here we assume waves propagate at the DJL speed, i.e., $c \approx c_{DJL}$, which includes the 10% uncertainty in $c$ into the calculation of $\Delta(z)$ (Figure 13, gray). If $c$ is close to $U_w$ then the 10% uncertainly would translate into much larger uncertainties in the transport distance [*Lamb*, 1997]. Additionally, the strongest transports would be expected to be up shallow, above our direct velocity measurements.

As a comparison, northerly wind off the WA coast generates an offshore wind-driven Ekman transport in the surface layer, leading to an onshore transport below the surface and near-shore coastal upwelling due

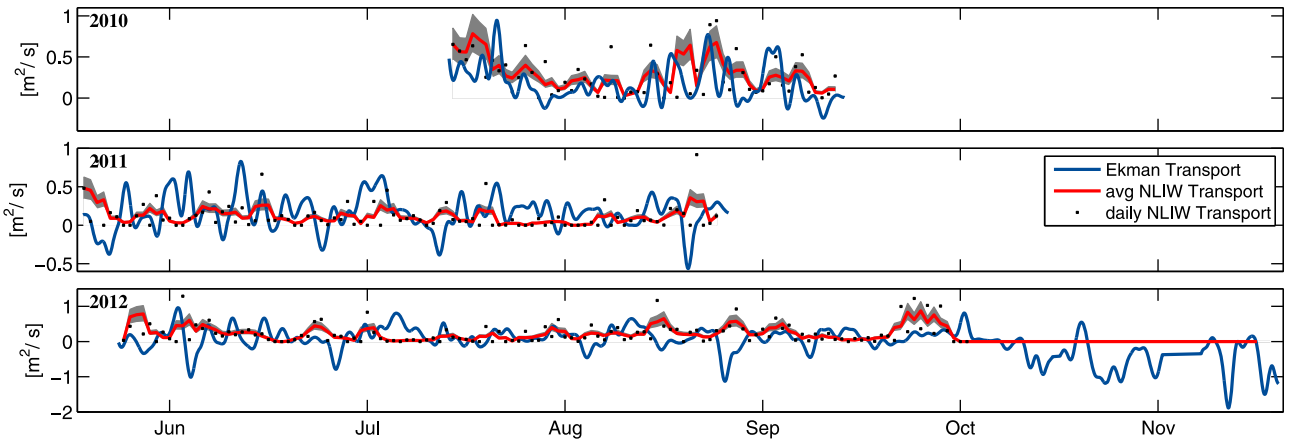


**Figure 13.** Three years (2010–2012) of the 1 day low-passed Ekman transport (blue lines), daily averaged onshore transport due to the NLIWs (black dots) and its moving average (red lines). Gray indicates error bars due to the 10% uncertainty in phase speed.

to mass conservation. The Ekman transport is calculated as $U_E = \tau_s/(\rho_0 f)$ [*Ekman*, 1905], where $\tau_s$ is the along-shelf component of the wind stress (Figure 2a), $\rho_0 = 1025 \mathrm{kgm}^{-3}$ is a nominal background density, and $f$ is the Coriolis parameter. Averaged over the upwelling periods, $U_E$ has a mean (median) of 0.21(0.15), 0.20 (0.15), and 0.19 (0.12) $\mathrm{m}^2\mathrm{s}^{-1}$ during *ChaBa* deployments in Year 2010, 2011, and 2012, respectively. Here $U_E$ is about one third smaller than the value off the Oregon coast [*Lentz*, 1992], as a result of the weak upwelling-favorable winds off the WA coast comparing to the rest of US West coast [*Hickey and Banas*, 2008]. Comparing the daily average NLIW transport to onshore Ekman transport balancing the surface-layer offshore transport in three years (Figure 13), the time-integrated effect of the strong but episodic NLIW transport is significant compared to the weak but sustained Ekman transport, making the waves a potentially important contributor to the local mass balance.

## 4. Discussion

Nonlinear internal waves observed in this study have a large variety of shapes and properties, including internal solitary waves, solitary wave trains and internal bores. The formation, evolution and breaking of NLIWs have been analyzed in previous numerical and laboratory studies, presumably depending on bathymetry features, tidal forcing, background stratification/currents and the earth's rotation [e.g., *Maxworthy*, 1980; *Helfrich and Melville*, 1986; *Legg and Adcroft*, 2003; *Venayagamoorthy and Fringer*, 2012]. The change in the relationship between these factors should lead to different evolution and dissipation as the wave propagates, thereby giving different shapes at the observational site [*Ostrovsky*, 1978; *Gerkema*, 1995; *Stepanyants*, 2006]. Additionally, variations in the oblique angle of incidence of the internal tides on the irregularly shaped continental shelf would be expected to modulate the formation and steepening of the waves. A full understanding of the generation and evolution of the NLIWs in the complicated coastal system with modulations/redirections by local low-frequency flows and bathymetry is beyond the scope of this study, and presumably requires more observational studies and three-dimensional, nonhydrostatic numerical simulations.

As shown, the nonlinear internal waves appear to transport water mass. The nitrate transport by nonlinear internal depression waves might be expected to be small because nitrate is minimum near the surface. However, the onshore mass transport due to NLIWs reaches a depth of ~20 m (Figure 12, bottom right), where the nitrate concentration is usually much higher than the surface layer. Assuming an offshore nitrate concentration of 1$\mu$M [*Banas et al.*, 2009] is transported by the waves onto a nitrate-free shelf, the onshore flux for a typical wave crest with an along-shelf length of 50 km is about 1.2 kg nitrate $\mathrm{s}^{-1}$ (assuming $U_T = 0.38\,\mathrm{m}^2\mathrm{s}^{-1}$, the time-average mass flux from previous section). Integrating the nitrate flux over the upwelling season (90 days), the total nitrate input due to NLIWs is up to $0.9\times10^7$ kg, about an order of magnitude smaller than the inputs from other sources, such as the Strait of Juan de Fuca, coastal water, canyon enhancement and the Columbia river [*Hickey and Banas*, 2008]. It is noted that this simple calculation is based on a number of assumptions and approximations, including constant nitrate concentrations inside

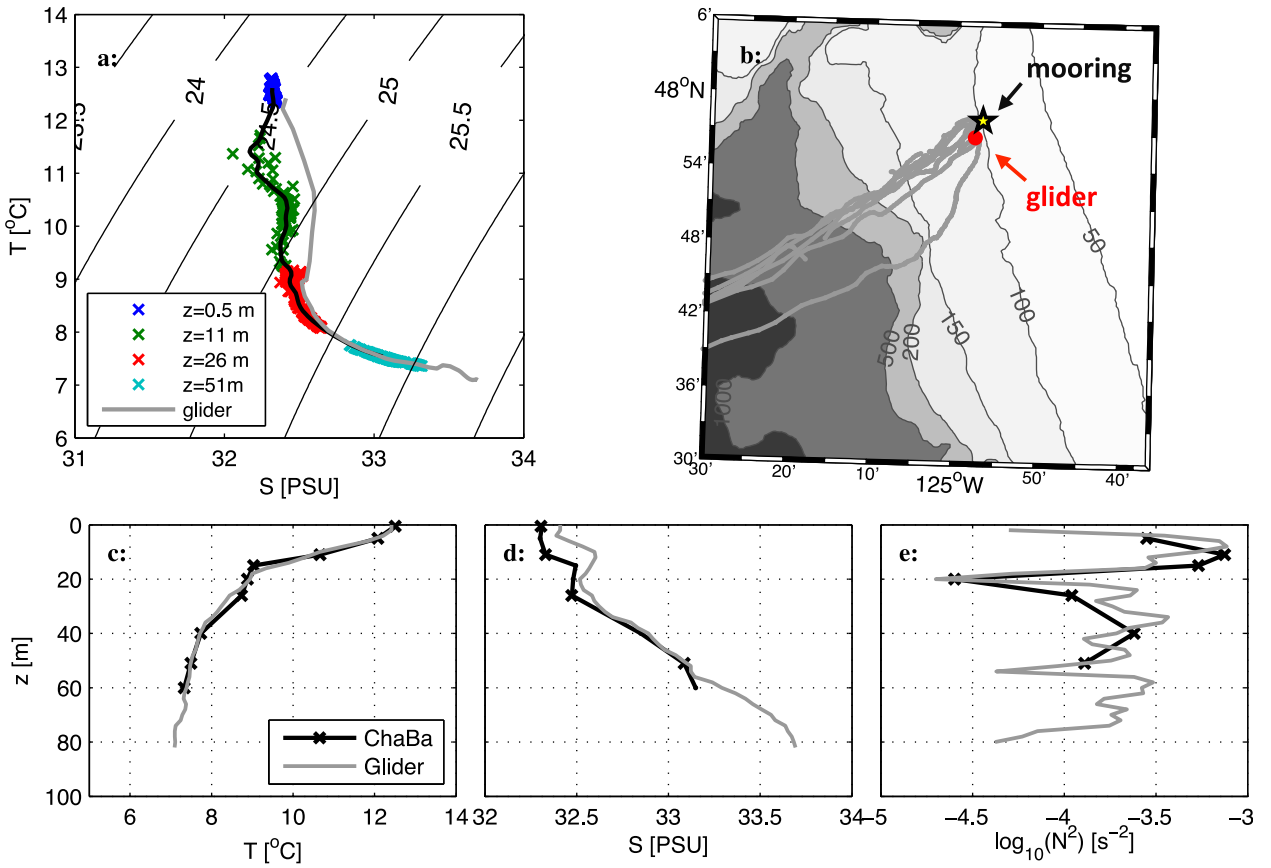


**Figure A1.** (a) A piece-wise linear fit of salinity using 3 h temperature (*T*) and salinity (*S*) measurements at depths 0.5, 11, 26 and 51 m on 9 August 2010, when the glider 2.8 km from the mooring (b, red dot); (b) Locations of the mooring (star), glider lines (gray lines) and the position of glider (profiles in Figure A1a); (c)–(e) comparing *T*, fitted *S*, and calculated stratification profiles from the mooring (black) and glider (gray), when the glider was at the position shown in Figure A1b.

wave crests and a linear relationship between $U_w$ and $\Delta(z)$ (which is a convex function according to *Lamb* [1997]). This near-surface transport would potentially be more significant to buoyant larvae or seeds of marine plants that need to be transported back onshore to settle. More detailed biogeochemical observations in the region are needed and are the focus of on-going work.

## 5. Conclusions

We document observed characteristics of nonlinear internal waves (NLIWs) on the Washington continental shelf, using four summers/falls of temperature, salinity and velocity records from a surface mooring. A large number ($>$ 1500) of NLIWs are detected and their taxonomy (internal solitary waves, solitary wave trains and internal bores) documented. Wave characteristics in the four years have similar features: onshore propagation directions toward the northeast; significant amplitudes relative to water depth (up to 51 m in 100 m water); and wave energy up to $\sim O(10^8\,\mathrm{J\,m^{-1}})$. Waves are generally weak in spring/early summer, strong in late summer/fall, and absent in winter, presumably due to variations in background stratification and currents that impact wave generation and propagation.

NLIWs appear to be generated by shoaling of remotely incident internal tides (IT) instead of by local barotropic conversion, suggested by (1) semidiurnal wave arrivals are often phase-locked with the internal tide; (2) the propagation direction of NLIWs and the IT energy flux direction are consistent, with NLIWs steered more onshore by the bathymetry; (3) NLIW and IT energy flux are correlated; and 4) NLIW energy flux and the local barotropic forcing are uncorrelated.

Estimated time-mean onshore transport due to NLIWs ($0.38\,\mathrm{m^2 s^{-1}}$) is significant compared to the Ekman transport, suggesting the waves may be an important mechanism for cross-shore mass transport during these periods. More detailed biogeochemical observations and modeling are required to estimate the effects of these waves on local nutrient supply and productivity.

## Appendix A: *T-S* Fit and Calculation of Stratification $N^2$

A piece-wise linearly-fitted *T-S* relationship is obtained every 3 h using time series of *T* and *S* at depths where both of them are sampled. The vertical motions of the waves during the 3 h period fill in the *T-S* space sampled at the finite depths (Figure A1, colored crosses). Values of *S* at depths lacking salinity measurements are estimated by *T* measurements along the fitted line (Figure A1a, black line). Buoyancy frequency $N=\sqrt{\frac{g}{\rho}\frac{d\rho}{dz}}$, where $g$ is the acceleration due to gravity, $\rho$ is the potential density, is calculated using observed and fitted *T*, *S* together. Full-depth *T*, *S* measurements from the glider when it was within 15 km of the mooring (Figure A1b) provides a validation of the calculation. The fitted *S* profile and calculated $N^2$ profile from the mooring are in agreement with the glider observations (Figures A1d and A1e). Note that the salinity offset in the upper 30 m (Figures A1a and A1d) is not a calibration error but a lateral gradient as displayed in the glider spatial measurements (not shown).

**Acknowledgments**

This work was supported in part by the National Oceanic and Atmospheric Administration (NOAA) under the US IOOS grant to NANOOS, NA11NOS0120036, and the National Science Foundation under grant OCE0968131. Data for this paper can be located at the following website: www.nanoos.org/nvs. The considerable hardware and instrumentation comprising the surface and subsurface moorings was purchased on a generous grant from the Murdock Charitable Trust. We thank three anonymous reviewers for their generous inputs. Thanks are extended to Barbara Hickey, Parker MacCready and Ryan McCabe for discussions on the Washington coastal environment and ecosystem; Ren-Chieh Lien and Frank *Henyey* for valuable discussions on the DJL model and trapped cores; Zhongxiang Zhao for helping with data analysis and suggestions on this paper; Mike Gregg, Jan Newton, Gunnar Voet, Barry Ma, Andy Pickering, Brian Chinn, Byron Kilbourne and Jun-Hong Liang for their generous and valuable discussions; the Captain and crew of the R/V Thomas G. Thompson for deploying and servicing the moorings; Eric Boget, Mike Carpenter, Sam Fletcher, Mike Kenney, Trina Litchendorf, Keith Magness, Tim McGinnis, Nick Michel-Hart, Zoë Parsons, Chris Siani and Tim Wen for the design and construction of the NEMO system; Craig Lee and his group for their assistance in piloting the glider; the U.S. Coast Guard station in La Push, Washington, for their hospitality and willingness to host our shore data station; the Quileute tribe for their support in onshore loading and the tribe marine biologist Jennifer Hagen for her contribution during cruises to deploy/recover ChaBa; and the Olympic Coast National Marine Sanctuary for their assistance and cooperation in glider and buoy logistics.

## References

Alford, M. H. (2003), Energy available for ocean mixing redistributed through long-range propagation of internal waves, *Nature*, *423*, 159–163.

Alford, M. H., and Z. Zhao (2007), Global patterns of low-mode internal-wave propagation, Part I: Energy and energy flux, *J. Phys. Oceanogr.*, *37*(7), 1829–1848.

Alford, M. H., R. Lien, H. Simmons, J. M. Klymak, Y. Yang, D. Tang, and M. Chang (2010), Speed and evolution of nonlinear internal waves transiting the South China Sea, *J. Phys. Oceanogr.*, *40*(6), 1338–1355.

Alford, M. H., J. B. Mickett, S. Zhang, Z. Zhao, and J. Newton (2012), Internal waves on the Washington continental shelf, *Oceanography*, *25*(2), 66–79.

Allen, S., and B. Hickey (2010), Dynamics of advection-driven upwelling over a shelf break submarine canyon, *J. Geophys. Res.*, *115*, C08018, doi:10.1029/2009JC005731.

Apel, J., L. Ostrovsky, Y. Stepanyants, and J. Lynch (2006), Internal solitons in the ocean, technical report, Woods Hole Oceanogr. Inst. Tech. Rept., WHOI-2006-04.

Baines, P. (1974), The generation of internal tides over steep continental slopes. *Philosophical Transactions of the Royal Society of London. Series A, Mathematical and Physical Sciences*, *277*(1263), 27–58.

Banas, N. S., E. Lessard, R. Kudela, P. MacCready, T. Peterson, B. Hickey and E. Frame (2009), Planktonic growth and grazing in the Columbia River plume region: A biophysical model study, *J. Geophys. Res.*, *114*, C00B06, doi:10.1029/2008JC004993.

Bogucki, D., T. Dickey, and L. Redekopp (1997), Sediment resuspension and mixing by resonantly generated internal solitary waves, *J. Phys. Oceanogr.*, *27*(7), 1181–1196.

Chang, M., R. Lien, Y. Yang, and T. Tang (2011), Nonlinear internal wave properties estimated with moored ADCP measurements, *J. of Atmos. Oceanic Technol.*, *28*(6), 802–815.

Colosi, J. A., R. C. Beardsley, J. F. Lynch, G. Gawarkiewicz, C. S. Chiu, and A. Scotti (2001), Observations of nonlinear internal waves on the outer New England continental shelf during the summer Shelfbreak Primer Study, *J. Geophys. Res.*, *106*(C5), 9587–9601.

D'Asaro, E., R. Lien, and F. Henyey (2007), High-frequency internal waves on the oregon continental shelf, *J. Phys. Oceanogr.*, *37*(7), 1956–1967.

Duda, T. F., J. F. Lynch, J. D. Irish, R. C. Beardsley, S. Ramp, C.-S. Chiu, T.-Y. Tang, and Y.-J. Yang (2004), Internal tide and nonlinear internal wave behavior at the continental slope in the northern South China Sea, *IEEE J. Oceanic Eng.*, *29*(4), 1–27.

Ekman, V. W. (1905), On the influence of the earth's rotation on ocean-currents, *Ark. Mat. Astron. Fys.*, *2*, 1–52.

Farmer, D. M., and L. Armi (1999), The generation and trapping of solitary waves over topography, *Science*, *283*, 188–190.

Farmer, D. M., and J. D. Smith (1980), Generation of lee waves over the sill in Knight Inlet, in *Fjord Oceanography*, edited by H. J. Freeland, D. M. Farmer, and C. Levings, pp. 259–269, Plenum, N. Y.

Gerkema, T. (1995), A unified model for the generation and fission of internal tides and solitary waves, *J. Mar. Res.*, *54*, 421–450.

Helfrich, K. R., and R. H. J. Grimshaw (2008), Nonlinear disintegration of the internal tide, *J. Phys. Oceanogr.*, *38*, 686–701.

Helfrich, K. R., and W. Melville (1986), On long nonlinear internal waves over slope-shelf topography, *J. Fluid Mech.*, *167*(1), 285–308.

Henyey, F. S. (1999), Exact solitary wave solutions in shallow water. Dynamics of Oceanic Internal Gravity Waves II: Proc. in *Aha Huliko'a Hawaiian Winter Workshop*, pp. 89–93, University of Hawaii at Manoa, Honolulu, HI.

Hickey, B. M. (1989), Patterns and processes of circulation over the Washington continental shelf and slope, *Elsevier Oceanogr. Ser.*, *47*, 41–115.

Hickey, B. M. (1995), Coastal submarine canyons, in *Proceedings Hawaiian Winter Workshop on Topographic Effects in the Ocean*, edited by P. Müller and D. Henderson, pp. 95–110, Hawaii Inst. of Geophys., Honolulu.

Hickey, B. M., and N. E. S. Banas (2008), Why is the northern California Current so productive?, *Oceanography*, *21*(4), 90.

Hickey, B. M., and N. S. Banas (2003), Oceanography of the U.S. Pacific Northwest coastal ocean and estuaries with application to coastal ecology, *Estuaries*, *26*(4B), 1010–1031.

Holliday, D., and M. E. McIntyre (1981), On potential energy density in an incompressible, stratified fluid, *J. Fluid Mech.*, *107*, 221–225.

Huthnance, J. M. (1995), Circulation, exchange and water masses at the ocean margin: The role of physical processes at the shelf edge, *Progr. Oceanogr.*, *35*(4), 353–431.

Inall, M., G. Shapiro, and T. Sherwin (2001), Mass transport by non-linear internal waves on the Malin Shelf, *Cont. Shelf Res.*, *21*(13), 1449–1472.

Inall, M. E., T. P. Rippeth, and T. J. Sherwin (2000), Impact of nonlinear waves on the dissipation of internal tidal energy at a shelf break, *J. Geophys. Res.*, *105*(C4), 8687–8705.

Kang, D., and O. Fringer (2010), On the calculation of available potential energy in internal wave fields, *J. Phys. Oceanogr.*, *40*(11), 2539–2545.

Klymak, J. M., and J. N. Moum (2003), Internal solitary waves of elevation advancing on a shoaling shelf, *Geophys. Res. Lett.*, *30*(20), 2045, doi:10.1029/2003GL017706.

Klymak, J. M., R. Pinkel, C. Teng Liu, A. K. Liu, and L. David (2006), Prototypical solitons in the South China Sea, *J. Geophys. Res.*, *33*, L11607, doi:10.1029/2006GL025932.
Lamb, K. (2002), A numerical investigation of solitary internal waves with trapped cores formed via shoaling, *J. Fluid Mech.*, *451*, 109–144.
Lamb, K. (2010), Energetics of internal solitary waves in a background sheared current, *Nonlinear Processes Geophys.*, *17*, 553–568.
Lamb, K. G. (1997), Particle transport by nonbreaking, solitary internal waves, *J. Geophys. Res.*, *102*(C8), 18,641–18,660.
Lamb, K. G. (2003), Shoaling solitary internal waves: On a criterion for the formation of waves with trapped cores, *J. Fluid Mech.*, *478*, 81–100.
Lamb, K. G. (2007), Energy and pseudoenergy flux in the internal wave field generated by tidal flow over topography, *Cont. Shelf Res.*, *27*(9), 1208–1232.
Lamb, K. G., and V. T. Nguyen (2009), Calculating energy flux in internal solitary waves with an application to reflectance, *J. Phys. Oceanogr.*, *39*(3), 559–580.
Lee, C.-Y. u., and R. C. Beardsley (1974), The generation of long nonlinear internal waves in a weakly stratified shear flow, *J. Geophys. Res.*, *79*(3), 453–462.
Legg, S., and A. Adcroft (2003), Internal wave breaking at concave and convex continental slopes, *J. Phys. Oceanogr.*, *33*(11), 2224–2246.
Lentz, S. J. (1992), The surface boundary layer in coastal upwelling regions, *J. Phys. Oceanogr.*, *22*(12), 1517–1539.
Lien, R., E. A. D'Asaro, F. Henyey, M. Huei Chang, T. Yung Tang, and Y.-J. Yang (2012), Trapped core formation within a shoaling nonlinear internal wave, *J. Phys. Oceanogr.*, *42*(4), 511–525.
Lien, R.-C., T. Y. Tang, M. H. Chang, and E. A. D'Asaro (2005), Energy of nonlinear internal waves in the South China Sea, *Geophys. Res. Lett.*, *32*, L05615, doi:10.1029/2004GL022012.
Lien, R.-C., T. B. Sanford, S. Jan, M.-H. Chang, and B. B. Ma (2013), Internal tides on the east china sea continental slope, *J. Mar. Res.*, *71*(1-2), 1–2.
Long, R. R. (1953), Some aspects of the flow of stratified fluids. I. A theoretical investigation, *Tellus*, *V*, 42–58.
MacFadyen, A., B. Hickey, and W. Cochlan (2008), Influences of the Juan de Fuca Eddy on circulation, nutrients, and phytoplankton production in the northern California Current System, *J. Geophys. Res.*, *113*, C08008, doi:10.1029/2007JC004412.
MacKinnon, J. A., and M. C. Gregg (2003), Mixing on the late-summer New England Shelf- Solibores, shear, and stratification, *J. Phys. Oceanogr.*, *33*, 1476–1492.
Maxworthy, T. (1980), On the formation of nonlinear internal waves from the gravitational collapse of mixed regions in two and three dimensions, *J. Fluid Mech.*, *96*(1), 47–64.
Moum, J., D. Farmer, E. Shroyer, W. Smyth, and L. Armi (2007a), Dissipative losses in nonlinear internal waves propagating across the continental shelf, *J. Phys. Oceanogr.*, *37*(7), 1989–1995.
Moum, J. N., D. M. Farmer, W. D. Smyth, L. Armi, and S. Vagle (2003), Structure and generation of turbulence at interfaces strained by internal solitary waves propagating shoreward over the continental shelf, *J. Phys. Oceanogr.*, *33*, 2093–2292.
Moum, J. N., J. M. Klymak, J. D. Nash, A. Perlin, and W. D. Smyth (2007b), Energy transport by nonlinear internal waves, *J. Phys. Oceanogr.*, *37*, 1968–1988.
Nash, J. D., M. H. Alford, and E. Kunze (2005), Estimating internal-wave energy fluxes in the ocean, *J. Atmos. Oceanic Technol.*, *22*(10), 1551–1570.
Nash, J. D., S. M. Kelly, E. L. Shroyer, J. N. Moum, and T. F. Duda (2012), The unpredictable nature of internal tides and nonlinear waves on the continental shelf, *J. Phys. Oceanogr.*, *42*(11), 1981–2000.
Ostrovsky, L. A. (1978), Nonlinear internal waves in the rotating ocean, *Oceanography*, *18*, 119–125.
Ostrovsky, L. A., and Y. Stepanyants (1989), Do internal solitons exist in the ocean?, *J. Geophys. Res.*, *27*, 2906–2926.
Pineda, J. (1991), Predictable upwelling and the shoreward transport of planktonic larvae by internal tidal bores, *Science*, *253*(5019), 548–551.
Pineda, J. (1999), Circulation and larval distribution in internal tidal bore warm fronts, *Limnol. Oceanogr.*, *44*, 1400–1414.
Scotti, A., and J. Pineda (2004), Observation of very large and steep internal waves of elevation near the Massachusetts coast, *Geophys. Res. Lett.*, *31*, L22307, doi:10.1029/2004GL021052.
Scotti, A., and J. Pineda (2007), Plankton accumulation and transport in propagating nonlinear internal fronts, *J. Mar. Res.*, *65*(1), 117–145.
Scotti, A., B. Butman, R. C. Beardsley, P. S. Alexander, and S. Anderson (2005), A modified beam-to-earth transformation to measure short-wavelength internal waves with an acoustic Doppler current profiler, *J. Atmos. Oceanic Technol.*, *22*, 583–591.
Scotti, A., R. Beardsley, and B. Butman (2006), On the interpretation of energy and energy fluxes of nonlinear internal waves: An example from Massachusetts Bay, *J. Fluid Mech.*, *561*, 103–112.
Scotti, A., R. Beardsley, B. Butman, and J. Pineda (2008), Shoaling of nonlinear internal waves in Massachusetts Bay, *J. Geophys. Res.*, *113*, C08031, doi:10.1029/2008JC004726.
Shroyer, E., J. Moum, and J. Nash (2010a), Energy transformations and dissipation of nonlinear internal waves over New Jersey's continental shelf, *Nonlinear Processes Geophys.*, *17*, 345–360.
Shroyer, E., J. Moum, and J. Nash (2011), Nonlinear internal waves over New Jersey's continental shelf, *J. Geophys. Res.*, *116*, C03022, doi:10.1029/2010JC006332.
Shroyer, E. L., J. N. Moum, and J. D. Nash (2010b), Vertical heat flux and lateral mass transport in nonlinear internal waves, *Geophys. Res. Lett.*, *37*, L08601, doi:10.1029/2010GL042715.
Stansfield, K. C., C. Garrett, and R. Dewey (2001), The probability distribution of the Thorpe displacement within overturns in Juan de Fuca Strait, *J. Phys. Oceanogr.*, *31*, 3421–3434.
Stanton, T. P., and L. A. Ostrovsky (1998), Observations of highly nonlinear internal solitons over the continental shelf, *Geophys. Res. Lett.*, *25*(14), 2695–2698, doi:10.1029/98GL01772.
Stastna, M., and K. Lamb (2002), Large fully nonlinear internal solitary waves: The effect of background current, *Phys. Fluids*, *14*, 2987.
Stepanyants, Y. (2006), On stationary solutions of the reduced Ostrovsky equation: Periodic waves, compaction and compound solitons, *Chaos Solitons Fractals*, *28*, 193–204.
Venayagamoorthy, S., and O. Fringer (2012), Examining breaking internal waves on a shelf slope using numerical simulations, *Oceanography*, *25*(2), 132–139.
Waterhouse, A. F., S. E. Allen, and A. W. Bowie (2009), Upwelling flow dynamics in long canyons at low Rossby number, *J. Geophys. Res.*, *114*, L08601, doi:10.1029/2010GL042715.
Winters, K. B., and R. Barkan (2013), Available potential energy density for Boussinesq fluid flow, *J. Fluid Mech.*, *714*, 476–488.